



Hierarchically phosphorus doped bimetallic nitrides arrays with unique interfaces for efficient water splitting



Feng-Cui Shen^{a,b}, Sheng-Nan Sun^a, Zhi-Feng Xin^a, Shun-Li Li^a, Long-Zhang Dong^a, Qing Huang^a, Yi-Rong Wang^a, Jiang Liu^{a,*}, Ya-Qian Lan^{a,*}

^a Jiangsu Key Laboratory of Biofunctional Materials, School of Chemistry and Materials Science, Nanjing Normal University, Nanjing, 210023, PR China

^b School of Biological and Chemical Engineering, Anhui Polytechnic University, Wuhu, 241000, PR China

ARTICLE INFO

Keywords:

Polyoxometalates
Bimetallic nitride
Electrocatalysis
Electrolysis of water
Stability

ABSTRACT

Engineering of nanomaterials with abundant interfaces is vital but remain challenges for the electrocatalysts of renewable energy conversion systems. Benefiting from the efficient synthetic approach, a high degree of controlled design can be attained for the first time in the synthesis of hierarchical catalysts P-NiMo₄N₅@Ni, in which different morphologies arrays on nickel foam (NF) were achieved via introducing polyoxometalates with the capability of controlling the nucleation and crystal growth. Especially, the optimized twist braid nitrides nanorod arrays electrode P-NiMo₄N₅@Ni-1 with high surface-to-volume ratio of energetic actives exhibited unprecedented activity as a bifunctional electrocatalyst for water splitting, approaching 50 and 100 mA cm⁻² at low cell voltages of 1.59 and 1.66 V, respectively, which is one of the best electrolytic water catalysts. The insights gained through this work may provide novel approach for designing other arrays derived from polyoxometalates with unique surfaces as versatile electrode and provide a design platform to prepare the invertible oxides catalysts from nitrides at high potential with enhanced catalytic performance.

1. Introduction

Controllable synthesis of electrode surface and interface has sparked researcher's intense interests due to the essential and effective function for optimizing the electrochemical activity of electrode materials [1–4]. Properly-defined surface and interface of electrode concentrated mainly on constructing the hierarchical and open structures, controlling the morphology of composites with high surface-to-volume ratio of actives for the effective mass and electron transport [5–7]. With respect to the water splitting driven by electricity with the sustainable production of inexhaustible hydrogen and oxygen [8], the approach electrolysis of water with low energy consumption and high electrical efficiency heavily relies on the innovative breakthroughs of designing the outstanding electrocatalysts for the two half reactions, hydrogen evolution reaction (HER) and oxygen evolution reaction (OER) [9]. Especially, OER electrocatalysts are prerequisite of the formidable bottleneck of water splitting due to the sluggish multielectron transfer process [10,11]. Great enthusiasm in exploring non-noble metal electrocatalysts has brought abundant achievements even surpassing the state-of-the-art catalysts Pt for HER and IrO₂ for OER [12,13]. Multiple researches presented some promising catalysts such as phosphides

[14,15], sulfide [16,17], selenides [18,19] nitrides [20–22], oxides [23,24], hydroxides [25,26] for HER or OER, but it remained a grand challenge to controllably prepare bifunctional catalysts with high reaction activity and electron conductivity for both HER and OER. Furthermore, the traditional catalysts are inclined to aggregate during pyrolysis and require additional polymeric binders to coat on a conductive substrate (carbon paper (CP), carbon cloth (CC), Ni foam (NF), etc.), which is greatly incommodeous for electron conductivity and bubbles release.

A tricky issue is how to monitor and design the microstructure of electrocatalysts for water splitting, in which the catalytic system presents a complex process evolving the three phase action between the electrode active material, the electrolyte and the generated gas. As the surface active sites of catalysts are energetic in electrocatalytic reaction [27], the promising strategy is to rational design multilevel structures with high surface-to-volume ratio for a quantity of catalytically active sites on multi-interfaces [26,28]. Notably, the controlled self-assembly of nanocomposites in the form of hierarchical superstructures such as nanosheets [29], nanowires [15], nanorods [30,31] and other nanotubes [32] arrays with oriented arrangement in situ grew on conductive substrate and acted as electrode directly, which markedly exposed

* Corresponding authors.

E-mail address: yqlan@njnu.edu.cn (Y.-Q. Lan).

catalytic sites along with effective gas release, mass and electron diffusions, thereby resulting in elevated electrochemical performances [33,34]. However, exploration of effective routes to realize the controllable growth of nanoarrays catalysts in the form of one-dimensional (1D) nanorod and two-dimensional (2D) nano-foliated structure anchored on three-dimensional (3D) NF are rarely developed due to the complexity intermolecular interface controls. Moreover, surface roughening of catalysts has weak bubble adhesion at the nanoarray electrode for the weak surface tension by affording the superaerophobic interface under water [35], which gives us the inspiration to controllably synthesis of arrays for different morphologies with abundant interfaces in the nano-scale level design.

Here, we report an original fabrication of P doped crystalline arrays NiMo_4N_5 supported on the Ni foam (P- NiMo_4N_5 @Ni) with controlled morphologies via a facile strategy adopting polymolybdcic acid and nickel nitrate as metal sources. Notably, $\text{H}_3\text{PMo}_{12}\text{O}_{40}$ (PMo₁₂) as Keggin-type POM has good water solubility and acidic properties, which could moderately dissolve a small amount of nickel on the surface of NF to form a homogeneous solution favorable for uniform arrays growth *in situ* and simultaneously introduce the heteroatomic P to the system. As a result, the self-supported binder-free electrode with the tailored 3D hierarchically architecture can be directly used to catalyze the OER and HER. Especially for the self-assemble P- NiMo_4N_5 @Ni-1 twist braid nanorod arrays electrode, it provided efficient electron conducting pathway and multiple interfaces exhibiting high bifunctional electrocatalytic activity toward HER and OER under alkaline conditions for the first time. Furthermore, our research discloses that $\text{NiMo}_4\text{O}_2\text{Ni}$ on the surface of P- NiMo_4N_5 @NF-1 serves as the active species for OER due to the oxidation *in situ*. When electrodes P- NiMo_4N_5 @Ni-1 were directly assembled as both cathode and anode for the electrolyzer, it exhibited surprising catalytic performance along with the long-term electrocatalytic stability, superior to most reported bifunctional electrocatalysts.

2. Material and methods

2.1. Synthesis of P- NiMo_4N_5 @Ni-1,2,3,4,5 and NiMo_4N_5 @Ni

Ni foams (NF) were washed ultrasonically for 10 min with acetone, water and ethanol two times each, respectively, and dried in an oven at 50 °C for use. In a typical procedure, a mixture of 0.1 mmol of phosphomolybdcic acid ($\text{H}_3\text{PMo}_{12}\text{O}_{41}\text{xH}_2\text{O}$), 0.6 mmol of nickel nitrate hexahydrate ($\text{Ni}(\text{NO}_3)_2\text{6H}_2\text{O}$) (atomic ratio Mo: Ni = 2:1) and 1 mmol urea ($\text{CO}(\text{NH}_2)_2$) were dissolved in water with continuous ultrasound for 20 min to obtain a clarified solution. Then the solution was transferred into Teflon-lined stainless-steel autoclave with a piece of pre-processed NF (1 cm × 2 cm) immersing it. The autoclave was maintained at 180 °C for 12 h and naturally cooled to room temperature. The resulting light yellow NF was washed with water and ethanol three times in turn and dried in an oven at 50 °C to obtain the nanorod arrays on NF as precursor. The amount of loading catalyst on NF was about 2.5 mg cm⁻². The precursor was subjected the ammoniated treatment at 500 °C for 4 h in NH_3 (150 ccm) reduction atmosphere to obtain the sample P- NiMo_4N_5 /Ni-1, whose mass loading is about 2.5 mg/cm².

P- NiMo_4N_5 @Ni-2,3 were obtained by the similar process with atomic ratio Mo:Ni (1:1) and Mo:Ni (1:2), respectively. P- NiMo_4N_5 @Ni-4,5 was also prepared similar with P- NiMo_4N_5 /Ni-1 without $\text{CO}(\text{NH}_2)_2$ and nickel source addition in the hydrothermal process. NiMo_4N_5 @Ni was gained by accepting molybdenum source $\text{NaMoO}_4\text{2H}_2\text{O}$ to replace $\text{H}_3\text{PMo}_{12}\text{O}_{41}\text{xH}_2\text{O}$ without P source.

2.2. Synthesis of Pt/C@Ni and IrO_2 @Ni

Similarly, the Pt/C@Ni and IrO_2 @Ni working electrodes were prepared by the following process. Firstly 2.5 mg catalyst Pt/C or IrO_2 was dispersed in 950 μL ethanol and 50 μL Nafion (1 wt.%) solution under

sonication for 30 min to form a homogeneous solution. Then, 100 μL solution was slowly loaded onto the preprocessed NFs and dried to obtain the working electrodes Pt/C@Ni and IrO_2 @Ni with the area loading 2.5 mg/cm².

2.3. Characterization

X-ray powder diffraction (XRD) measurements were characterized on a D/max 2500 V L/PC diffractometer equipped with graphite monochromatized $\text{Cu K}\alpha$ radiation ($\lambda = 1.54060 \text{ \AA}$). Scanning electron microscopy (SEM) images and Energy dispersive X-ray spectroscopy (EDS) were conducted by a JSM-7600 F apparatus with an acceleration voltage of 10 kV to character the morphology of samples. Transmission electron microscopy (TEM) images were recorded on JEOL-2100 F instrument with an acceleration voltage of 200 kV. High-resolution TEM (HRTEM) images, Energy dispersive X-ray spectroscopy (EDS) and corresponding elemental mapping were carried on JSM-5160LV-Vantage typed energy spectrometer. Fourier transform infrared spectroscopy (FTIR) was conducted on a Mattson Alpha-Centauri spectrometer. X-ray photoelectron spectroscopy (XPS) was recorded on scanning X-ray microprobe (PHI 5000 Verasa, ULAC-PHI, Inc.) employing Al $\text{K}\alpha$ radiation and C1 s peak at 284.8 eV as an internal standard.

2.4. Electrochemical measurements

All electrochemical measurements were conducted on the autolab workstation (Biologic) in a typical three-electrode configuration at room temperature. The as-prepared samples were directly used as working electrode with Ag/AgCl (saturated potassium chloride) and graphite rod as reference and counter electrodes, respectively.

Linear sweep voltammetry (LSV) scans for HER and OER were conducted at a scan rate of 5 mV s⁻¹ in 1 M KOH between 0.1 to -0.8 V and 1–2 V vs. RHE, respectively. All the LSV data were acquired till the stable polarization curves were obtained after several CV cycles.

The durability for HER and OER was executed by the chronamperometry at the corresponding overpotential to the current density of 10 mA cm⁻² for HER and 50 mA cm⁻² for OER up to 24 h. The durability for water splitting was also performed by the chronamperometry at the corresponding potential to the current density for 24 h.

Electrochemical double layer capacitance evaluations were carried out via CV method at non-faradaic potentials range from 1.2 to 1.3 V vs RHE with different scan rates: 20, 40, 60, 80, 100, 120, 140 mV s⁻¹. By plotting the ΔJ at the potential of 1.25 V vs RHE against the scan rate, the linear slope C_{dl} is used to represent the ECSA.

The overall water splitting was conducted in a two-electrode system, comprising of P- NiMo_4N_5 /Ni-1 as both anode and cathode electrode. The polarization curves were obtained by linear sweep voltammetry in the potential range of 1–2 V vs RHE at a scan rate of 5 mV s⁻¹ in 1 M KOH. Faradic efficiency was performed by adopting the electrolysis in a sealed electrochemical H-type cell at the corresponding potential to the current density of 50 mA cm⁻². The gaseous generated by water electrolysis was detected by a gas chromatography (GC-7920), H_2 and O_2 was monitored by the thermal conductivity detector (TCD) with nitrogen as the carrier gas.

The calculation of Faradaic efficiency

$$\text{FE} = \alpha n F/Q \times 100\%$$

where α is the electron transfer number. n is the moles of the generated gas and F is the Faraday constant, Q represents the corresponding electric quantity.

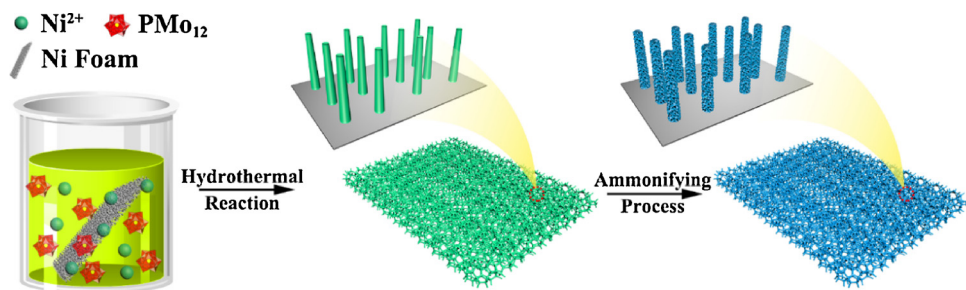


Fig. 1. Schematic illustration of the synthetic process of twist braid nanorod arrays P-NiMo₄N₅@Ni-1 composite.

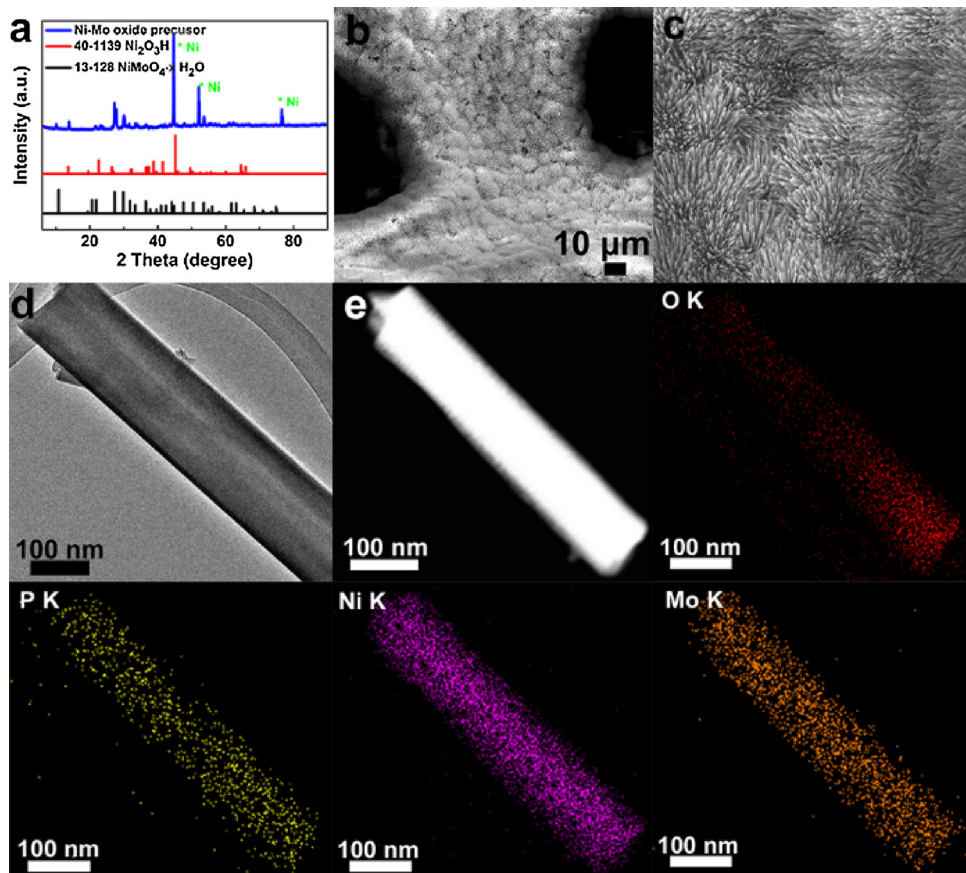


Fig. 2. Characterization of Ni-Mo oxide precursor of P-NiMo₄N₅-1. (a) XRD patterns of the precursor. (b) and (c) SEM images of precursor under different magnifications. (d) TEM image and (e) EDX elemental mapping of Ni-Mo oxide precursor of P-NiMo₄N₅-1.

3. Results and discussion

3.1. Structural and morphological characterization

The synthesis of the electrocatalyst was illustrated in Fig. 1 with two-step procedure. First, Ni–Mo oxide precursor slippy nanorod arrays were prepared via a hydrothermal reaction by a mixed solution containing PMo₁₂, Ni(NO₃)₂ with atom ratio 1:2 of nickel and molybdenum, urea (0.01 mol) and a piece of Ni foam (NF, 1*2 cm²) at 180 °C for 12 h. Owing to the action of PMo₁₂, the soluble small amount of Ni²⁺ ions from NF tend to concentrate at the substract surfaces where the reaction prefers to obtain the nanorod arrays perpendicularly grown on the NF. Second, when the as-synthesized precursors were calcined in the NH₃ atmosphere at 700 °C for 4 h, the formed twist braid nanorod arrays NiMo₄N₅ directly vertically aligned on NF and recorded as P-NiMo₄N₅@Ni-1. Some controlled samples were prepared for comparison. To clarify the effect of different compositions on electrochemical performances, the as-synthesized samples were also prepared and

denoted as P-NiMo₄N₅@Ni-2 (n_{Ni} : n_{Mo} = 1:1), P-NiMo₄N₅@Ni-3 (n_{Ni} : n_{Mo} = 2:1) and P-NiMo₄N₅@Ni-4 (n_{Ni} : n_{Mo} = 1:2 without urea) after the nitriding process. We also tried to use NF as both Ni source and self-supported 3D integrated skeletons, whose nitrides denoted as P-NiMo₄N₅@Ni-5. In order to further get insight into the influence of molybdenum source to the electrochemical properties, sodium molybdate was applied as the precursor instead of PMo₁₂ and the corresponding nitrides was noted as NiMo₄N₅@Ni.

First, X-ray diffraction (XRD; Fig. 2a) of the composite Ni-Mo oxide precursor gave signals for the crystalline NiMoO₄·xH₂O (JCPDS no. 13-128) and Ni₂O₃H (JCPDS no. 40-1139). Then we carried out ICP-AES on the pure oxide, which were carefully mechanically removed from the Ni foam, which gave a Ni/Mo ratio of 5.2:1.8 (Table S1), resulting in that the composition of NiMoO₄·xH₂O and Ni₂O₃H is close to 1:1. Scanning electron microscopy (SEM) (Fig. 2b, c) and transmission electron microscopy (TEM) images (Fig. 2d) scrutinized that oxide precursor was constructed of oriented nanorod arrays with smooth surface, diameters ranging between 100–120 nm and lengths about 5–10 μm uniformly

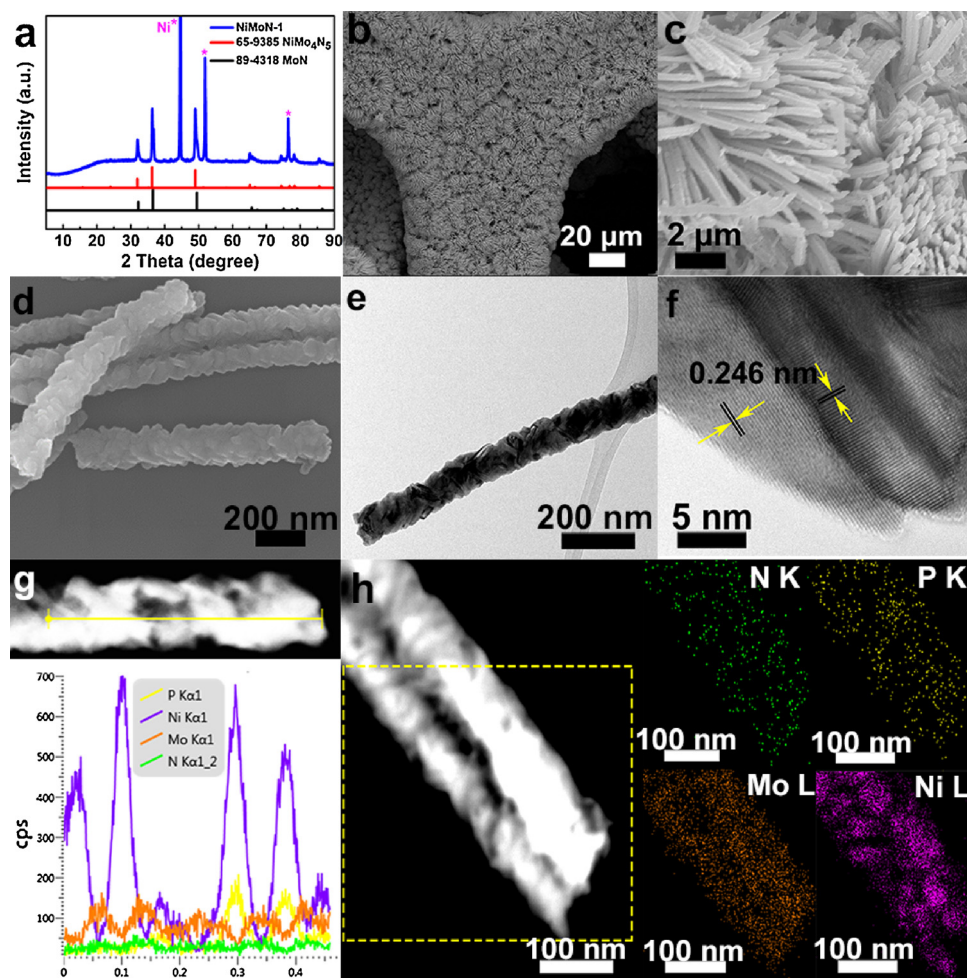


Fig. 3. Characterization of P-NiMo₄N₅@Ni-1. (a) XRD patterns of the composite P-NiMo₄N₅@Ni-1. (b), (c) and (d) SEM images of P-NiMo₄N₅@Ni-1 under different magnifications. (e) TEM and (f) HRTEM images of P-NiMo₄N₅@Ni-1. EDX elemental mapping of (g) linear scan and (h) plane sweep of N, P, Mo and Ni for P-NiMo₄N₅@Ni-1.

aligned on NF. Furthermore, the element mapping of the high-angle annular dark-field scanning transmission electron microscopy (HAADF-STEM) in Fig. 2e manifested the uniform distribution of elements in nanorods prepared by hydrothermal method.

The crystalline structures of different nitride samples were also identified by XRD, Fig. 3a and Figure S1 in the Supporting Information). Results reveal the as-obtained peaks resulting from the crystalline NiMo₄N₅ (JCPDS no. 65-9385) and Ni (JCPDS no. 1-1258). Interestingly, the original morphology of nanorod arrays was well maintained (Fig. 3b), but the surface changed to form twist braid nanorods with unique interfaces shown by SEM (Fig. 3c, d) and TEM (Fig. 3e) images after annealing in a reduction ammonia atmosphere for 4 h, which may attribute that most oxygen atoms in arrays were near the surface and could be easily replaced by nitrogen atoms for a thermodynamically stable structure in the ammonia reduction environments [35]. Besides, the twist braid nanorod array morphology was further proofed by linear scanning of Energy dispersive X-ray spectrometry (EDS, Fig. 3g) with special zigzag graphics. High-resolution TEM (HRTEM) image in Fig. 3 f clearly showed the lattice spacing of 0.246 nm, corresponding to the (100) plane of NiMo₄N₅ (JCPDS no. 65-9385). Interestingly, the precursors of P-NiMo₄N₅@Ni-2 and P-NiMo₄N₅@Ni-3 exhibited layers laminated of nanoflower arrays (Fig. 4a, b) and tremella-like thin nanosheet arrays (Fig. 4c, d), respectively, which may ascribe that high concentrations of Ni source significantly facilitate the growth of crystal nucleation along the flakes. Their corresponding morphologies changed little after the ammoniation treatment (Figure S2a and S3a). The

element mapping measurements were also executed out on the nanorod or nanosheet peeled from P-NiMo₄N₅@Ni-1 (Fig. 3h), P-NiMo₄N₅@Ni-2 (Figure S2c) and P-NiMo₄N₅@Ni-3 (Figure S3c) manifesting P, N, Ni and Mo elements are all homogeneously distributed in line with the Energy dispersive X-ray spectrometry (EDS, Figure S4) and embodying the uniformity of different arrays by hydrothermal method. In the control experiment of P-NiMo₄N₅@Ni-1, irregular nanorod arrays shape (Figure S5a) were obtained in P-NiMo₄N₅@Ni-4 when there is no urea adding while irregular bulk shape (Figure S5c) in P-NiMo₄N₅@Ni-5 were achieved when NF acted as the nickel source in the precursor preparation. There is no obvious change in the corresponding morphology after ammoniation treatment (Figure S5b, 5d). When sodium molybdate was used as the molybdenum source, acicular arrays of NiMo₄N₅@Ni were irregularly distributed on NF in Figure S5e. Worse still, some samples were removed from the skeleton after ammoniation treatment (Figure S5f).

3.2. Electrocatalytic activity

3.2.1. HER performance of catalysts

The catalytic activity of P-NiMo₄N₅@Ni-1 for HER was evaluated employing a three-electrode configuration in 1 M KOH and was compared to Pt/C@Ni and bare NF (Fig. 5a). Notably, all the curves were demonstrated without iR correction including the real resistive loss in the catalytic process. The polarization curve of P-NiMo₄N₅@Ni-1 delivered a relatively low overpotential of 118 mV at the current density

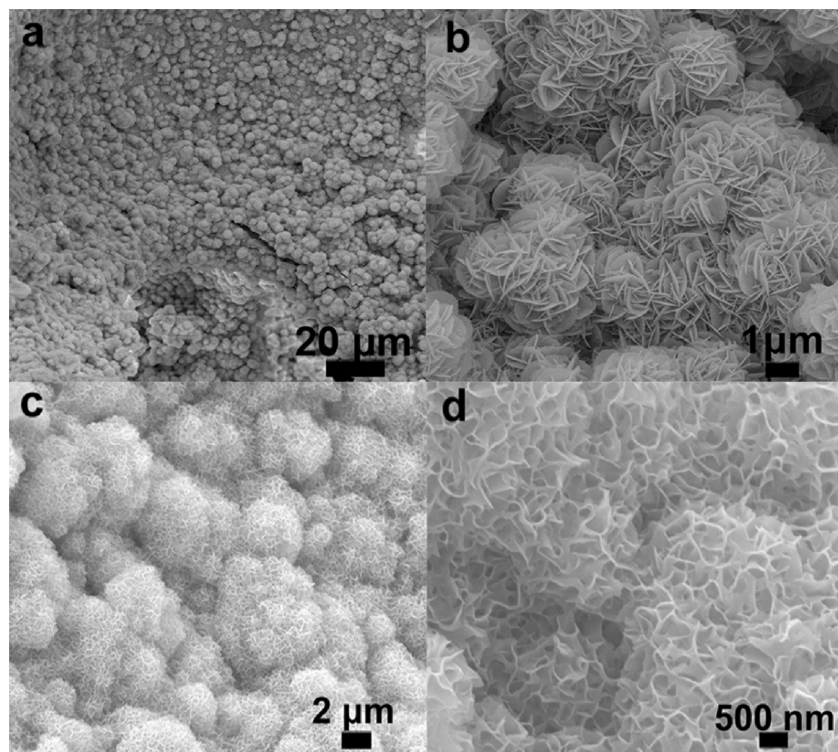


Fig. 4. SEM images of (a) precursor of P-NiMo₄N₅@Ni-2 and (b) under different magnifications, (c) precursor of P-NiMo₄N₅@Ni-3 and (d) under different magnifications.

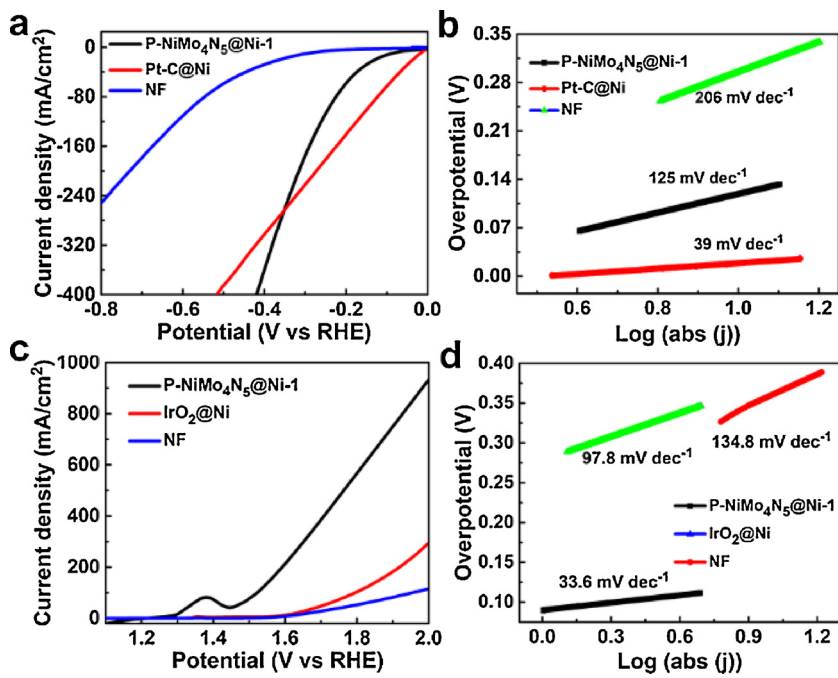


Fig. 5. Electrochemical performances of electrocatalysts. (a) Polarization curves of catalysts for HER and (b) corresponding Tafel plots. (c) Polarization curves of catalysts for OER and (d) corresponding Tafel plots. All the experiments were conducted in 1 M KOH at room temperature.

of 10 mA cm⁻² (η_{10}), which greatly outperformed that of NF (296 mV) even better than Pt/C@NF at relatively high potentials giving large current densities. The superior activity may due to the fact that nitrogen atoms modulated d-band density of positively charged Ni and Mo atoms contributing the similar electronic structures with noble metals of group VIII [36]. Tafel plots were constructed from the polarization curves to evaluate the catalytic activity from a kinetic viewpoint. As expected, P-NiMo₄N₅@Ni-1 manifested a small Tafel slope of 125 mV

dec⁻¹ higher than Pt/C@Ni (39 mV dec⁻¹) but evidently lower than bare Ni foam (296 mV dec⁻¹) in Fig. 5b. To further give sight in the effect of ammoniated treatment on the activity of catalyst, we compared the performance of precursor of P-NiMo₄N₅@Ni-1 and P-NiMo₄N₅@Ni-1 in Figure S6a and S6b. As can be seen, precursor of P-NiMo₄N₅@Ni-1 have inferior property, which manifested the favorable performance for the nitrides adjusting the density of metal d-band to realize vacancy defect and thus improving the ability to supply

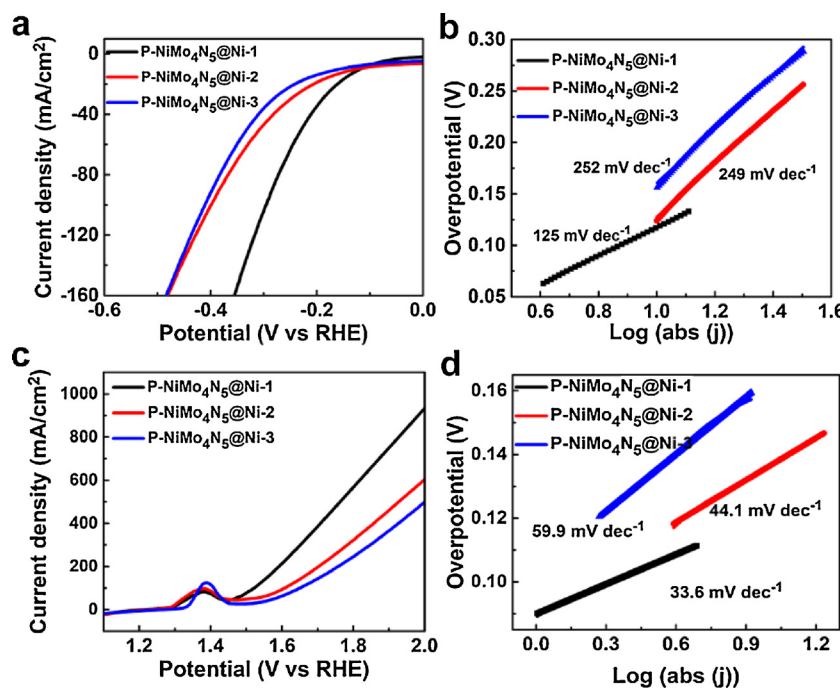


Fig. 6. Electrochemical performances of electrocatalysts. (a) Polarization curves of catalysts with different atom ratio of nickel and molybdenum for HER and (b) corresponding Tafel plots. (c) Polarization curves of catalysts with different atom ratio of nickel and molybdenum for OER and (d) corresponding Tafel plots.

electrons for electrolytic water. The electrocatalytic activity of different nickel and molybdenum element molar ratio for nitrides toward HER was evaluated in Fig. 6a. The corresponding overpotentials required for η_{100} are 123 and 156 mV for P-NiMo₄N₅@Ni-2 and P-NiMo₄N₅@Ni-3 (Fig. 6b), respectively. The results showed that the HER activity decreased with the decreasing level of molybdenum source, which may ascribe that nickel–molybdenum based composites combined two non-noble metals from an ascending branch with weaker Ni–H bonds and a descending branch with stronger Mo–H bonds of volcano curve generating enhanced activity for HER [37–39]. We also tested the HER polar curves and corresponding Tafel plot of P-NiMo₄N₅@Ni-4,5 constructed by different precursors (Figure S7a, S7b). Obviously, the performance of P-NiMo₄N₅@Ni-4 and P-NiMo₄N₅@Ni-5 for HER was influenced by the irregular nanorods and bulk morphology, which greatly decreased the specific surface area for contacting the electrolyte and thus weakened the corresponding performance. NiMo₄N₅@Ni obtained inferior catalytic performance for HER acquiring high overpotential of 221 mV at η_{100} and Tafel plot of 172 mV dec⁻¹, which manifested the effect of P doping and regular morphology on electrochemical performance. Comparatively, P-NiMo₄N₅@Ni-1 obtained superior performance attributing to two aspects. On the one hand, P doping modified the electronic properties of nitrides and created more active sites. On the other hand, P-NiMo₄N₅@Ni-1 had uniformly twist braid nanorod morphology with large specific surface to immerse the electrolyte and thus improved its electrocatalytic activity [40].

3.2.2. OER performance of catalysts

The OER as the bottle-neck reaction in many energy devices hinders the development of energy storage and conversation due to its multistep proton-coupled sluggish electron transfer processes. The OER activity of P-NiMo₄N₅@Ni-1 was also estimated by a three electrode device in 1.0 M KOH and compared to precious metal catalysts IrO₂@Ni and bare NF. The polarization curves in Fig. 5c manifested the well-known oxidation peak of NiOOH from Ni(OH)₂ at about 1.38 V and the performance of P-NiMo₄N₅@Ni-1 exhibited a fairly higher activity than that of IrO₂@Ni and bare NF. Specifically, the 3D hierarchical electrode achieved the current densities of 100 mA cm⁻² (η_{100}) requiring the overpotential of 297 mV and even superior to the most highly catalytic

activity of non-noble metal OER catalysts (Table S2). In contrast, state of the art IrO₂@Ni and bare NF electrodes exhibited poor performance with the overpotentials of 554 and 625 mV at η_{100} , respectively. Furthermore, the P-NiMo₄N₅@Ni-1 electrode showed a fairly small Tafel slope among the catalysts (Fig. 5d). In stark contrast, the particular low Tafel slope value of 33.6 mV dec⁻¹ for P-NiMo₄N₅@Ni-1 indicated fast kinetics of O₂ evolution representing the inherent OER activity. The catalytic activities achieved by bimetallic composites P-NiMo₄N₅@Ni-1 are tremendous, which may due to different metal species modulation of gas adsorption energy and improvement of electronic conductivity [13,41]. For comparison, precursor of P-NiMo₄N₅@Ni-1 was carried out for OER approaching the overpotential of 435 mV at η_{100} and Tafel slope of 65 mV dec⁻¹ (Figure S6c and Figure S6d), and further indicated the superiority of nitride P-NiMo₄N₅@Ni-1. Control sample P-NiMo₄N₅@Ni-2,3 were also used for OER with the overpotential of 370 and 420 mV at η_{100} , and Tafel slope of 44.1 and 59.9 mV dec⁻¹ (Fig. 6c, d), respectively. Their inferior catalysts activity may ascribe that the congregated nanoflowers and nanosheets of P-NiMo₄N₅ easily folded and stacked during the high temperature processing (Figure S2a and Figure S3a) providing less accessible catalytic sites. Furthermore, unstable morphologies also hindered its performance, which was verified by the SEM images of post-OER P-NiMo₄N₅@Ni-2,3 (Figure S8a and Figure S8b). Similarly, P-NiMo₄N₅@Ni-4,5 and P-NiMo₄N₅@Ni obtained poor performance with the overpotential of 403, 426 and 498 mV at η_{100} , and Tafel slope of 49.4, 53.6 and 58.2 mV dec⁻¹ (Figure S7c, 7d), respectively, illustrating the positive effect of uniform morphology and P doping.

To investigate the effective electrochemically active surface area (ECSA) of various morphologies during OER catalysis, cyclic voltammetry (CV) with different scan rates was carried out to estimate the double-layer capacitance (Cdl). The comparison of Cdl values (Fig. 7) indicates that the active surface area of P-NiMo₄N₅@Ni-1 is higher than that of P-NiMo₄N₅@Ni-2, P-NiMo₄N₅@Ni-3. The high surface area attributed to the controlled nanorod arrays and subsequent unique twist braid nanorod structure with more interfaces after the annealing processes, whose hierarchical structure was favorable for the intimate accessibility of electrolyte, exposed more active sites for electrochemical reactions and thus promoted the electrochemical activity in alkaline

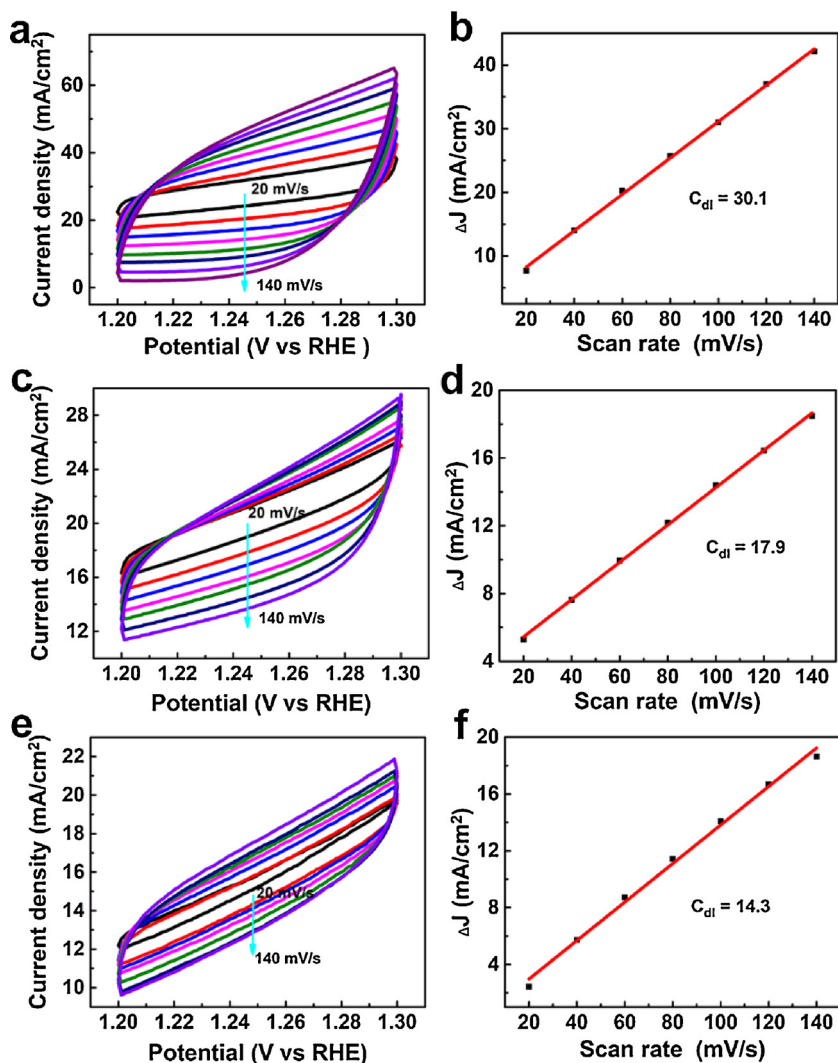


Fig. 7. Electrochemical activity specific surface area of different catalysts. (a), (c) and (e) CV of P-NiMo₄N₅@Ni-1,2,3 with different rates from 20 to 140 mV s⁻¹, (b), (d) and (f) ΔJ of catalysts P-NiMo₄N₅@Ni-1,2,3 plotted against scan rates at the potential of 1.25 V vs RHE. The slopes were used to denote the ECSA.

medium.

Electrochemical impedance spectroscopy (EIS) was carried out to provide essential insights into the electrode kinetics during electrochemical catalysis process in Figure S9. The as-prepared vertical P-NiMo₄N₅@Ni-1 retained a vast interconnected structure on NF providing greater electrochemically active surface area to expose abundant reaction sites than that of the accumulated P-NiMo₄N₅@Ni-2 and P-NiMo₄N₅@Ni-3, which was more benefit for the transfer of electrons and protons, thus decreased the electrochemical impedance.

3.2.3. Stability of electrode P-NiMo₄N₅@Ni-1

High durability of catalysts are also crucial issues for electrochemical reaction due to the corrosive potential. Expectedly, the P-NiMo₄N₅@Ni-1 also show good durability for HER and OER proved by the chronoamperometric measurements (Fig. 10a), in which negligible current decay is detected upon the 24 h operation with the corresponding overpotential of η_{10} and η_{50} . Furthermore, the morphology of P-NiMo₄N₅@Ni-1 still remains as nanorod arrays after the HER and OER measurement (Fig. 8b, c, d), demonstrating the structural integrity of 3D nanorods can still be maintained during the process of repeated bubbles aggregation and release. Then we carried out the XRD characterization of P-NiMo₄N₅@Ni-1 after the electrochemical tests (Fig. 8a). Obviously, The XRD pattern of post-HER P-NiMo₄N₅@Ni-1 have no changes in the characteristic peaks. While, the intensity of

characteristic peaks in post-OER P-NiMo₄N₅@Ni-1 may due to the formation of new composite on the surface. To confirm the compositional element change, EDX elemental mapping of P-NiMo₄N₅@Ni-1 after the electrochemical test for OER was conducted on the pure nanorods which were mechanically removed from the Ni foam (Fig. 8e). There are a small amount of N and P elements on the surface of the nanorods, but also a small amount of O elements, which further indicates that the composition changes during the catalytic process.

As recent studies showed that transition metal nitrides may undergo unobtrusive component changes and convert into the corresponding metal hydroxides/oxides at high voltage for OER [42]. So some surface structure sensitive characterizations were performed to give some insight in the changes of the catalytic active species P-NiMo₄N₅@Ni-1 after OER. We carried out the X-ray photoelectron spectroscopy (XPS) to trace the elemental composition and valence changes of surface elements in the P-NiMo₄N₅@Ni-1 before and after the oxidation process (Fig. 9). As can be seen, N, P, Ni and Mo elements existed in the as prepared sample P-NiMo₄N₅@Ni-1 before the OER reaction. The high-resolution N 1s spectra were fitted into two peaks at 395.02 and 397.82 eV revealing the existence of Mo-N and Ni-N [43]. The P 2p spectrum deconvoluted into two peaks with binding energy of 129.8 and 133.8 eV assigning to phosphide and phosphate signals [44]. The peaks in high-resolution XPS spectra of Ni 2p located at 852.4 and 869.5 eV attributing to Ni²⁺, the others at 855.6 and 873.3 eV

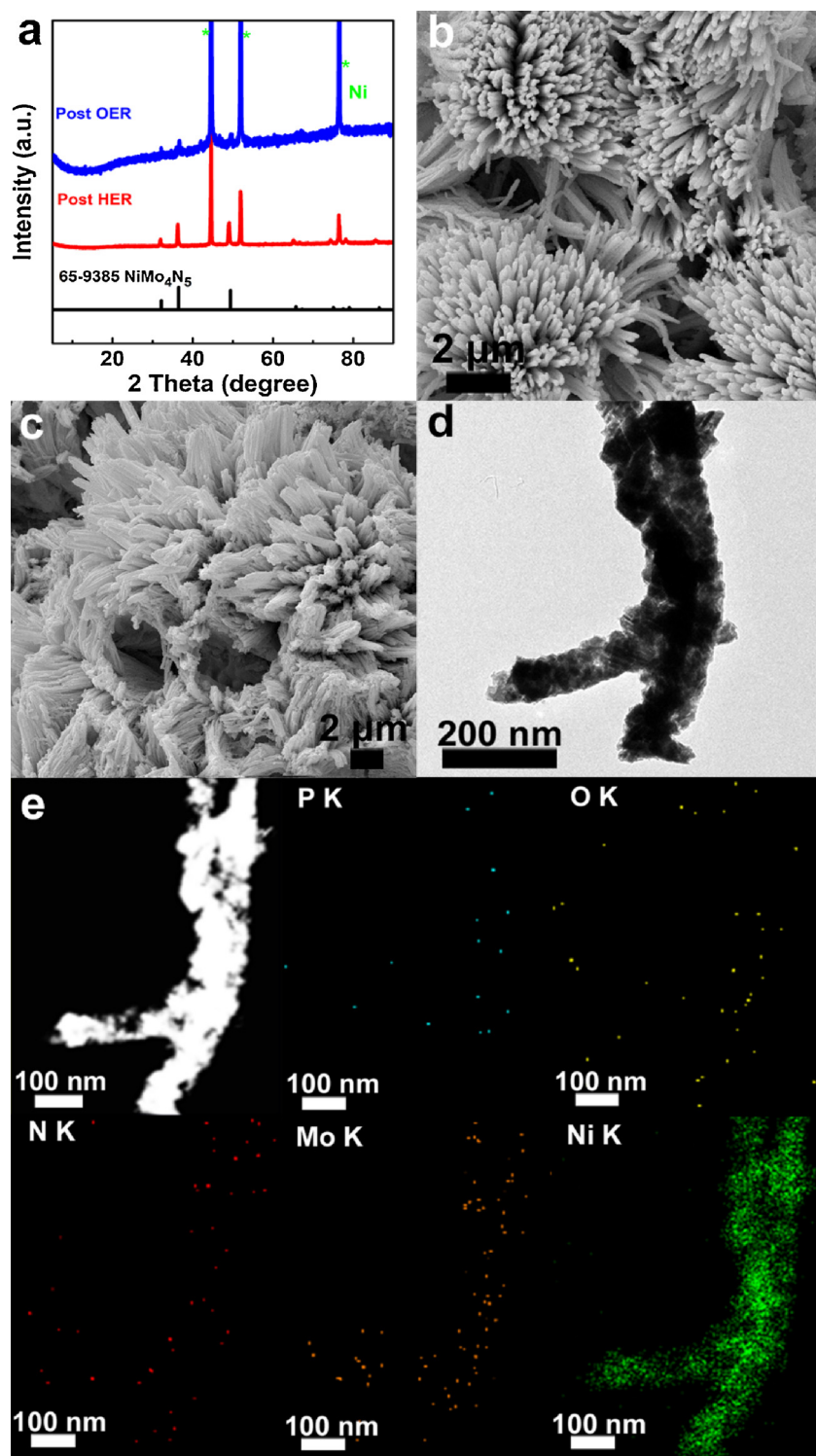


Fig. 8. Characterization of P-NiMo₄N₅@Ni-1 after electrochemical tests. (a) XRD patterns of P-NiMo₄N₅@Ni-1 after tests, (b) SEM of P-NiMo₄N₅@Ni-1 after electrochemical test for HER, (c) SEM, (d) TEM and (e) EDX elemental mapping of P-NiMo₄N₅@Ni-1 after the electrochemical test for OER.

accompanied by two satellite peaks corresponded to Ni²⁺ [25]. In the Mo 3d spectrum, two characteristic peaks at 232.5 and 229.2 eV are ascribed to Mo⁴⁺ and the other pair of peaks at 235.9 and 233.2 eV confirmed the presence of the Mo⁶⁺ assigning to the surface oxidation of Mo [43]. After the OER, the spectrum of Ni 2p is positively shifted displaying four peaks of Ni²⁺ (856.6 and 874.9 eV) and NiOOH (855.7 and 873.1 eV) [45], respectively, and signifying the coexistence of Ni²⁺ and Ni³⁺ species after the oxidation. Similarly, the peaks around 234.4,

230.9, 235.6 and 232.1 eV for Mo 2p were attributed to Mo⁵⁺ and Mo⁶⁺ after the OER [46]. Fourier transform infrared spectra (FT-IR) further affirmed the presence of MoO_x in Figure S10 for the characteristic peaks at ~ 1385 , ~ 824 and $\sim 634\text{ cm}^{-1}$. Based on the above analysis, the resulting active sites on the surface of the electrode for OER may be the oxidized catalyst MoNi-O-@Ni derived from the P-NiMo₄N₅@Ni-1. The conversion is so fast that there is no obvious current change in the durability test (Fig. 10 a).

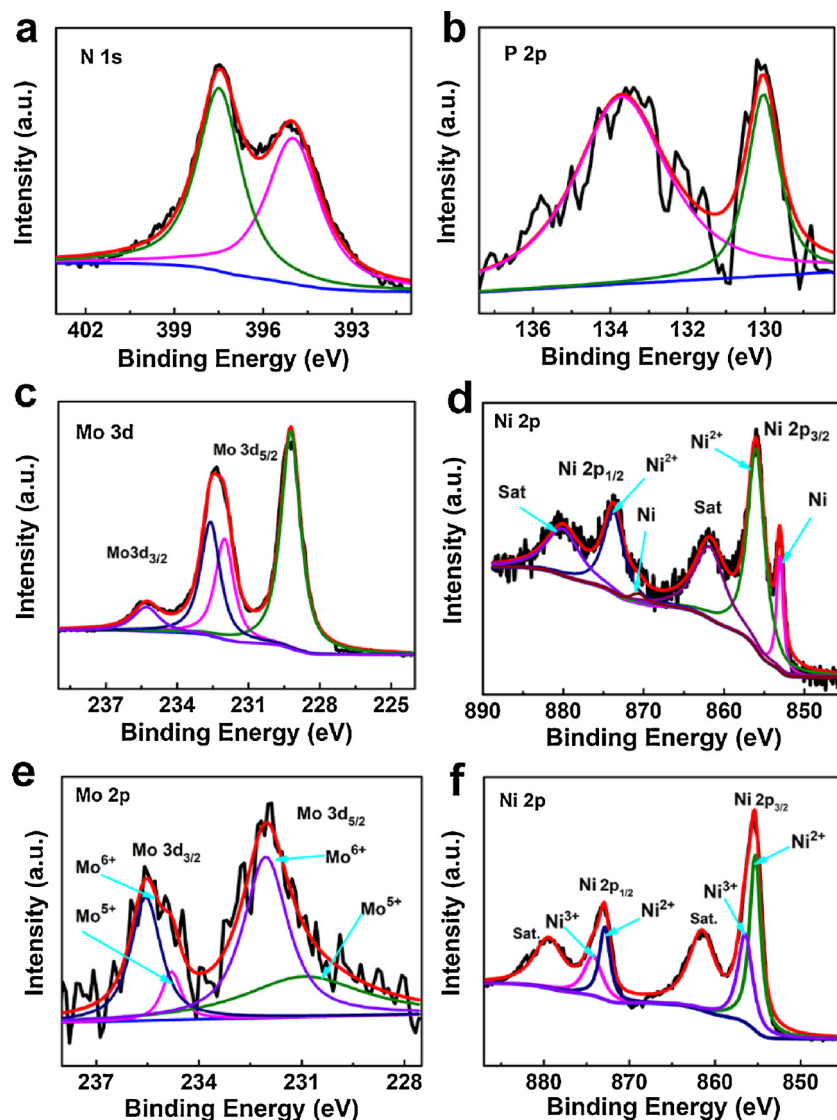


Fig. 9. XPS spectrum of electrode P-NiMo₄N₅@Ni-1. XPS high-resolution scans of (a) N 1 s, (b) P 2 P, (d) Mo 2 P, (e) Ni 2 P before the chronoamperometric test for OER. XPS high-resolution scans of (e) Mo 2 P, (f) Ni 2 P after the chronoamperometric test for OER.

3.2.4. The performance of the electrolysis water of symmetric electrode P-NiMo₄N₅@Ni-1

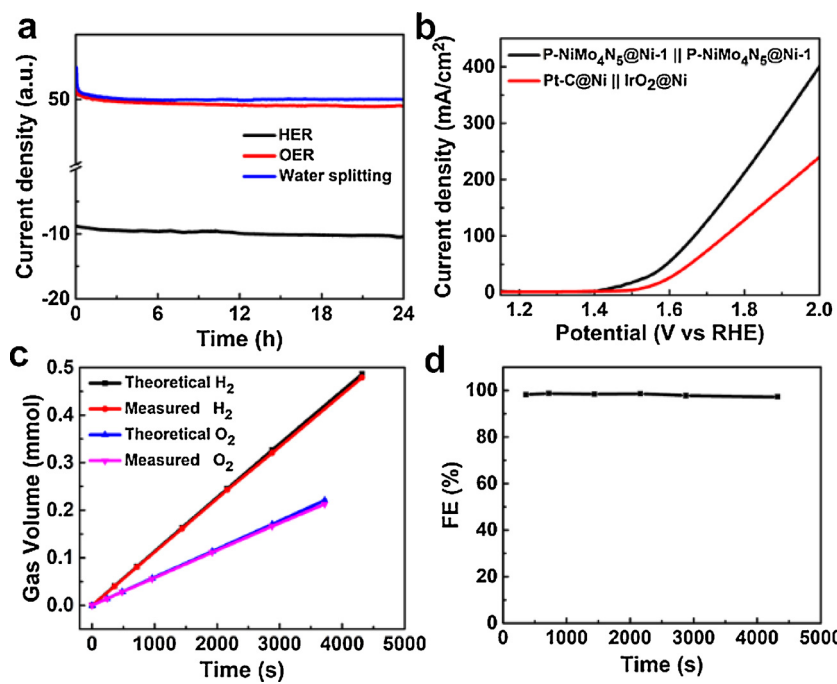
Inspired by the superior bifunctional electrocatalytic performance of P-NiMo₄N₅@Ni-1 towards HER and OER, we fabricated an electrolyzer to evaluate the overall water splitting performance, comprising P-NiMo₄N₅@Ni-1 electrode as both the cathode and anode. For comparison, control electrolyzer was also assembled by using the state of the art Pt/C and IrO₂ catalysts both combined on NF (IrO₂@Ni||Pt/C@Ni) with the same loading of P-NiMo₄N₅@Ni-1 as cathode and anode. As shown in Fig. 10b, the P-NiMo₄N₅@Ni-1||P-NiMo₄N₅@Ni-1 electrode can achieve η_{100} at the voltage of 1.66 V which are better than that of IrO₂@Ni||Pt/C@Ni electrode and most of nonprecious metal catalysts (Table S3). Furthermore, P-NiMo₄N₅@Ni-1 also has a good durability for water electrolysis at a fixed current density of 50 mA cm⁻² (Fig. 10a), which meets the requirements of practical application. The moles of released hydrogen and oxygen bubbles was plotted with the coincidence of theoretically calculated value in Fig. 10c. Correspondingly, nearly 100% of faradaic efficiency in Fig. 10d was obtained by comparing the amount of gas generated experimentally with theoretical value, manifesting the electrolysis has almost no side effects.

Such remarkable catalytic activity of the P-NiMo₄N₅@Ni-1 could be due to the following factors: (1) The hierarchical architecture of 1D

highly active nanorod arrays vertically grew on 3D conductive substrate NF ensures good electrical contacts without additional binders benefiting for the efficient mass and electron transfer. (2) The unique twist braid structures with plentiful interfaces facilitate small bubbles generation and detaching from the electrode. (3) P-NiMo₄N₅@Ni-1 has high intrinsically catalytic activities for HER and their surface can be easily transformed into NiMo-O@Ni active species for the OER. The above synergistic electronic interactions of bimetallic nitrides and oxides together may make a big contribution for water electrolysis performance.

4. Conclusions

In conclusion, the confined NiMo₄N₅@Ni arrays with controllable morphologies were achieved by introducing the polyoxometalates into array synthesis for the first time and the following simple ammoniation process, in which the exposed large specific surface area endowed these architectures with richness activity. Especially, the as-synthesized P-NiMo₄N₅@Ni-1 possesses twist braid hierarchical structure with multiple interfaces featuring the avoidable active sites aggregation, large specific surface area and high electronic conduction beneficial for energy conversion. The unique morphology coupled with intrinsic



catalytic activity of P doping bimetallic nitride NiMo₄N₅ resulted the outstanding performance for electrolysis of water far exceeding most of electrocatalysts and long-term electrocatalytic stability for at least 24 h. This work sets a refined method to explore other multi-interface electrocatalysts in nanoscale for water splitting and gives the fundamental investigation of the transition of nitrides catalysts at high potential catalysis. Furthermore, in view of the simple preparation and remarkable catalytic performance, the integrated electrode P-NiMo₄N₅@Ni-1 advances the practical research for alkaline electrolyzers.

Acknowledgements

This work was financially supported by NSFC (No. 21622104, 21471080 and 2170010097), the NSF of Jiangsu Province of China (No. SBK2017040708), the Natural Science Research of Jiangsu Higher Education Institutions of China (No. 17KJB150025), Priority Academic Program Development of Jiangsu Higher Education Institutions and the Foundation of Jiangsu Collaborative Innovation Center of Biomedical Functional Materials.

Appendix A. Supplementary data

Supplementary material related to this article can be found, in the online version, at doi:<https://doi.org/10.1016/j.apcatb.2018.10.012>.

References

- [1] K.X. Wang, X.H. Li, J.S. Chen, *Adv. Mater.* 27 (2017) 527–545.
- [2] J. Wang, H. Tang, L. Zhang, H. Ren, R. Yu, Q. Jin, J. Qi, D. Mao, M. Yang, Y. Wang, P. Liu, Y. Zhang, Y. Wen, L. Gu, G. Ma, Z. Su, Z. Tang, H. Zhao, D. Wang, *Nat. Energy* 1 (2016) 16050.
- [3] L. Peng, Z. Fang, Y. Zhu, C. Yan, G. Yu, *Adv. Energy Mater.* 8 (2018) 1702179.
- [4] S. Chai, Y.J. Wang, Y.-N. Zhang, H.Y. Zhao, M.C. Liu, G.H. Zhao, *Appl. Catal. B: Environ.* 237 (2018) 473–481.
- [5] P. Wang, X. Zhang, J. Zhang, S. Wan, S. Guo, G. Lu, J. Yao, X. Huang, *Nat. Commun.* 8 (2017) 14580.
- [6] K. Fan, Y. Ji, H. Zou, J. Zhang, B. Zhu, H. Chen, Q. Daniel, Y. Luo, J. Yu, L. Sun, *Angew. Chem. Int. Ed.* 56 (2017) 3289–3293.
- [7] M. Monai, T. Montini, E. Fonda, M. Crosara, J.J.D. Jaen, G. Adami, P. Fornasiero, *Appl. Catal. B: Environ.* 236 (2018) 88–98.
- [8] A. Ambrosi, M. Pumera, *Adv. Funct. Mater.* 28 (2017) 1700655.
- [9] Y. Hou, M.R. Lohe, J. Zhang, S. Liu, X. Zhuang, X. Feng, *Energy Environ. Sci.* 9 (2016) 478–483.
- [10] J. Huang, J. Chen, T. Yao, J. He, S. Jiang, Z. Sun, Q. Liu, W. Cheng, F. Hu, Y. Jiang, Z. Pan, S. Wei, *Angew. Chem. Int. Ed.* 54 (2015) 8722–8727.
- [11] X. Zhao, X.Q. Li, Y. Yan, Y.L. Xing, S.C. Lu, L.Y. Zhao, S.M. Zhou, Z.M. Peng, J. Zeng, *Appl. Catal. B: Environ.* 236 (2018) 569–575.
- [12] J.S. Li, Y. Wang, C.H. Liu, S.L. Li, Y.G. Wang, L.Z. Dong, Z.H. Dai, Y.F. Li, Y.Q. Lan, *Nat. Commun.* 7 (2016) 8.
- [13] F.-C. Shen, Y. Wang, Y.-J. Tang, S.-L. Li, Y.-R. Wang, L.-Z. Dong, Y.-F. Li, Y. Xu, Y.-Q. Lan, *ACS Energy Lett.* 2 (2017) 1327–1333.
- [14] K. Xu, H. Cheng, H. Lv, J. Wang, L. Liu, S. Liu, X. Wu, W. Chu, C. Wu, Y. Xie, *Adv. Mater.* 30 (2018) 1703322.
- [15] J. Li, G. Wei, Y. Zhu, Y. Xi, X. Pan, Y. Ji, I.V. Zatovsky, W. Han, *J. Mater. Chem. A* 5 (2017) 14828–14837.
- [16] P. Chen, T. Zhou, M. Zhang, Y. Tong, C. Zhong, N. Zhang, L. Zhang, C. Wu, Y. Xie, *Adv. Mater.* 29 (2017) 1701584.
- [17] C. Guan, X. Liu, A.M. Elshahawy, H. Zhang, H. Wu, S.J. Pennycook, J. Wang, *Nanoscale Horiz.* 2 (2017) 342–348.
- [18] W. Li, X. Gao, D. Xiong, F. Wei, W.-G. Song, J. Xu, L. Liu, *Adv. Energy Mater.* 7 (2017) 1602579.
- [19] X. Xu, F. Song, X. Hu, *Nat. Commun.* 7 (2016) 12324.
- [20] B. Zhang, C. Xiao, S. Xie, J. Liang, X. Chen, Y. Tang, *Chem. Mater.* 28 (2016) 6934–6941.
- [21] W.-F. Chen, K. Sasaki, C. Ma, A.I. Frenkel, N. Marinkovic, J.T. Muckerman, Y. Zhu, R.R. Adzic, *Angew. Chem. Int. Ed.* 51 (2012) 6131–6135.
- [22] Y. Zhang, B. Ouyang, J. Xu, G. Jia, S. Chen, R.S. Rawat, H.J. Fan, *Angew. Chem. Int. Ed.* 55 (2016) 8670–8674.
- [23] Y.P. Zhu, T.Y. Ma, M. Jaroniec, S.Z. Qiao, *Angew. Chem. Int. Ed.* 56 (2017) 1324–1328.
- [24] R. Ge, M. Ma, X. Ren, F. Qu, Z. Liu, G. Du, A.M. Asiri, L. Chen, B. Zheng, X. Sun, *Chem. Commun.* 53 (2017) 7812–7815.
- [25] L. Yu, H. Zhou, J. Sun, F. Qin, F. Yu, J. Bao, Y. Yu, S. Chen, Z. Ren, *Energy Environ. Sci.* 10 (2017) 1820–1827.
- [26] S. Niu, W.-J. Jiang, T. Tang, Y. Zhang, J.-H. Li, J.-S. Hu, *Adv. Sci.* 4 (2017) 1700084.
- [27] G. Zhu, R. Ge, F. Qu, G. Du, A.M. Asiri, Y. Yao, X. Sun, *J. Mater. Chem. A* 5 (2017) 6388–6392.
- [28] T. Tang, W.J. Jiang, S. Niu, N. Liu, H. Luo, Y.Y. Chen, S.F. Jin, F. Gao, L.J. Wan, J.S. Hu, *J. Am. Chem. Soc.* 139 (2017) 8320–8328.
- [29] D. Zhou, Z. Cai, X. Lei, W. Tian, Y. Bi, Y. Jia, N. Han, T. Gao, Q. Zhang, Y. Kuang, J. Pan, X. Sun, X. Duan, *Adv. Energy Mater.* 8 (2018) 1701905.
- [30] J. Zhang, T. Wang, P. Liu, Z.Q. Liao, S.H. Liu, X.D. Zhuang, M.W. Chen, E. Zschech, X.L. Feng, *Nat. Commun.* 8 (2017) 8.
- [31] Y.-Y. Chen, Y. Zhang, X. Zhang, T. Tang, H. Luo, S. Niu, Z.-H. Dai, L.-J. Wan, J.-S. Hu, *Adv. Mater.* 29 (2017) 1703311.
- [32] J.-X. Feng, H. Xu, Y.-T. Dong, S.-H. Ye, Y.-X. Tong, G.-R. Li, *Angew. Chem. Int. Ed.* 55 (2016) 3694–3698.
- [33] Y.J. Li, H.C. Zhang, M. Jiang, Q. Zhang, P.L. He, X.M. Sun, *Adv. Funct. Mater.* 27 (2017) 8.
- [34] L.-B. Huang, L. Zhao, Y. Zhang, Y.-Y. Chen, Q.-H. Zhang, H. Luo, X. Zhang, T. Tang, L. Gu, J.-S. Hu, *Adv. Energy Mater.* 8 (2018) 1800734.
- [35] N. Han, K.R. Yang, Z. Lu, Y. Li, W. Xu, T. Gao, Z. Cai, Y. Zhang, V.S. Batista, W. Liu, X. Sun, *Nat. Commun.* 9 (2018) 924.
- [36] Z. Lv, M. Tahir, X. Lang, G. Yuan, L. Pan, X. Zhang, J.-J. Zou, *J. Mater. Chem. A* 5 (2017) 20932–20937.

[37] Y. Zhang, X. Xia, X. Cao, B. Zhang, N.H. Tiep, H. He, S. Chen, Y. Huang, H.J. Fan, *Adv. Energy Mater.* 7 (2017) 1700220.

[38] J. Tian, N. Cheng, Q. Liu, X. Sun, Y. He, A.M. Asiri, *J. Mater. Chem. A* 3 (2015) 20056–20059.

[39] M. Fang, W. Gao, G. Dong, Z. Xia, S. Yip, Y. Qin, Y. Qu, J.C. Ho, *Nano Energy* 27 (2016) 247–254.

[40] J. Hassoun, K.-S. Lee, Y.-K. Sun, B. Scrosati, *J. Am. Chem. Soc.* 133 (2011) 3139–3143.

[41] D. Friebel, M.W. Louie, M. Bajdich, K.E. Sanwald, Y. Cai, A.M. Wise, M.-J. Cheng, D. Sokaras, T.-C. Weng, R. Alonso-Mori, R.C. Davis, J.R. Bargar, J.K. Nørskov, A. Nilsson, A.T. Bell, *J. Am. Chem. Soc.* 137 (2015) 1305–1313.

[42] S. Jin, *ACS Energy Lett.* 2 (2017) 1937–1938.

[43] Y. Zhu, G. Chen, X. Xu, G. Yang, M. Liu, Z. Shao, *ACS Catal.* 7 (2017) 3540–3547.

[44] P. Jiang, Q. Liu, Y. Liang, J. Tian, A.M. Asiri, X. Sun, *Angew. Chem. Int. Ed.* 53 (2014) 12855–12859.

[45] A.N. Mansour, C.A. Melendres, *Surf. Sci. Spectra* 3 (1994) 271–278.

[46] X.-X. Li, F.-C. Shen, J. Liu, S.-L. Li, L.-Z. Dong, Q. Fu, Z.-M. Su, Y.-Q. Lan, *Chem. Commun.* 53 (2017) 10054–10057.